Applied Environmental Research (2026) 48(2), 014
https://doi.org/10.35762/AER.2026014

Applied Environmental Research
- RESEARCH FOR SUSTAINABLE PLANET -

Research Article

Microwave-assisted Synthesis of Fe_2O_3/Mn_2O_3/rGO Nanocomposite for Effective Remediation of Parathion Pesticide under Visible Light Illumination

Nguyen V. N. Mai[1], Pham N. Chuc[2,*], Nguyen H. Chi[3], Nguyen M. Phuong[3], Nguyen Q. Bac[2], Nguyen T. H. Chi[2], Dao N. Nhiem[2,4], Nguyen T. Kien[2,4,*]

[1] *Faculty of Science, Quy Nhon University, 170 An Duong Vuong Street, Quy Nhon Nam Ward, Gia Lai, Vietnam*
[2] *Institute of Materials Science, Vietnam Academy of Science and Technology, 18 Hoang Quoc Viet Street, Nghia Do Ward, Hanoi, Vietnam*
[3] *Faculty of Chemistry, VNU University of Science, Vietnam National University, 19 Le Thanh Tong Street, Cua Nam Ward, Hanoi, Vietnam*
[4] *Graduate University of Science and Technology, Vietnam Academy of Science and Technology, 18 Hoang Quoc Viet Street, Hanoi, Vietnam*

*Corresponding Email: chucpn@ims.vast.ac.vn, nguyentrungkien1009@gmail.com

Abstract

Organophosphorus compounds are effective pesticides and insecticides but are also persistent and highly hazardous. In this work, a Fe_2O_3/Mn_2O_3/reduced-graphene-oxide (FM/rGO) composite was utilized as a photocatalyst for the degradation of parathion, a typical organophosphorus pesticide. The cost-effective and environmentally friendly FM/rGO material was prepared by a coprecipitation method assisted by microwave irradiation and characterized by various techniques, including X-ray diffraction (XRD), scanning electron microscopy (SEM), transmission electron microscopy (TEM), and UV–Vis spectroscopy. Compared with pristine Fe_2O_3 and Mn_2O_3, the immobilization of Fe_2O_3 and Mn_2O_3 on the rGO support significantly enhanced the photodegradation of parathion, primarily by reducing the recombination rate of the photogenerated electron–hole pairs. The FM/rGO achieved approximately 100% degradation of parathion within 45 min and mineralized nearly 90% of the initial parathion after 150 min under visible light irradiation. In addition, FM/rGO exhibited outstanding durability and recyclability, with only a 5% reduction in degradation efficiency after seven consecutive cycles.

ARTICLE HISTORY

Received: 7 Oct. 2025
Revised: 19 Jan. 2026
Accepted: 24 Feb. 2026
Published: 10 Mar. 2026

KEYWORDS

Organophosphorus;
Parathion;
Fe_2O_3/Mn_2O_3/rGO,
Photocatalyst

Introduction

Agriculture cannot do without herbicides and pesticides; it helps people avoid weeds and pests. They assist individuals in preventing the proliferation of weeds and insects, hence influencing agricultural productivity. However, the use of doses exceeding the permissible threshold for a long time can cause pollution in that area, severely affecting the soil, water environment, and people living there, especially when the pesticide cannot evaporate or decompose by itself.

Parathion is a highly toxic organophosphorus pesticide that is widely used in agricultural applications and has been banned and restricted in most countries because of its detrimental effects on environmental quality and human health. Parathion and its oxidative transformation products, particularly paraoxon, exhibit strong environmental persistence and can accumulate in soil and aquatic systems, thereby contributing significantly to pesticide pollution in agricultural regions (Ahmad and Mehmood, 2022). To process these persistent organic compounds, environmental researchers and remediators have used methods to recover and degrade them. To address these persistent organic compounds, researchers and remediators have used methods such as electrochemistry (Loučka et al., 2018), oxidation (Liao et al., 2025), and photocatalysis (Herrmann and Guillard, 2000) to recover and decompose them. Currently, photocatalysis is a common method for the

degradation of organic contaminants; it uses metal oxide materials, which are inexpensive and environmentally friendly and have high decomposition efficiency. For example, according to Kim et al. (2006), a TiO_2-based photocatalyst has been reported to be effective for parathion degradation, achieving the removal of parathion within 60 minutes and over 90% TOC reduction after 150 minutes.

α-Fe_2O_3 is among the most popular and least expensive catalyst materials. α- Fe_2O_3 has a relatively narrow band gap of 2.0–2.2 eV, enabling absorption of visible light up to approximately 600 nm and utilization of nearly 40% of the solar spectrum. Compared with other transition metal oxides, α- Fe_2O_3 is highly stable in aqueous environments with pH values above 3, making it suitable for long-term operation under photocatalytic and photoelectrochemical conditions (Mishra, and Chun, 2015). Importantly, its band gap (~2.1 eV) is smaller than the oxidation potential of water, which allows for efficient photogenerated hole transfer to water molecules and makes it a promising candidate for photodoped water oxidation and pollutant degradation.

Despite these advantages, hematite still suffers from several intrinsic drawbacks, including a short hole diffusion length (2–4 nm), poor electrical conductivity, and slow oxygen evolution, which together limit its overall photocatalytic efficiency (Jha et al., 2024; Jha and Jang, 2025). To address these limitations, extensive research has been devoted to structural and compositional modifications, such as nanostructuring, elemental doping, surface modification, and heterojunction construction with other semiconductors or carbon-based materials, which have been widely explored. For example, doping with oxides such as TiO_2 or Mn_xO_y can effectively tailor the band gap, improve the charge carrier mobility, and enhance the light absorption capacity (Choudhary et al., 2021; Kumar et al., 2020; Mohamed et al., 2020).

In addition, graphene-based compounds such as graphene oxide (GO) or reduced graphene oxide (rGO) have been employed for effective catalytic processes (Mondal et al., 2021; Li et al., 2016; Usgodaarachchi et al., 2023). The good electrical conductivity and extensive surface area enabled those materials to function as electron acceptors and transport mediators, facilitating charge separation. By capturing photogenerated electrons from the conduction band and reducing recombination rates with holes in the valence band, GO and rGO significantly extend the lifetime of charge carriers. This synergistic effect not only promotes interfacial charge transfer but also improves the overall photocatalytic activity of Fe_2O_3-based nanocomposites.

Photocatalytic materials based on Fe_2O_3 continue to attract significant research interest owing to their favorable properties and affordability. To overcome the intrinsic limitations of hematite, researchers have developed a variety of heterogeneous material systems incorporating Fe_2O_3 with other functional components, such as Fe_3O_4, Fe_2O_3/TiO_2 composites (Singh et al., 2019), $Fe_2O_3/ZnFe_2O_4/ZnO$ (Choudhary et al., 2021), and Fe_2O_3/Mn_xO_y systems, such as spinel magnesium ferrite (MFO) (Le et al., 2024).

In this article, a Fe_2O_3/Mn_2O_3/rGO (FM/rGO) nanocomposite was synthesized by a coprecipitation method assisted by microwave irradiation. The prepared samples were then characterized by XRD, SEM, TEM, and DRS before the photocatalytic activities were tested with parathion under simulated visible light.

Materials and methods

1) Chemicals

$Fe(NO_3)_3{\cdot}9H_2O$, $Mn(NO_3)_2$ solution (50%), graphite, $KMnO_4$, $NaNO_3$, H_2O_2 (30%), H_2SO_4 (98%), and polyvinyl alcohol (PVA) were purchased from Xilong Scientific Co., Ltd. Absolute alcohol (99,6%) was purchased from Duc Giang Chemicals Co., Ltd. Parathion ($C_{10}H_{14}NO_5PS$) was obtained from Merck.

2) Synthesis of rGO and FM/rGo

2.1) Synthesis of rGO

GO was obtained by the Hummers method (Sohail et al., 2017). Initially, H_2SO_4 was cooled to 0 °C, after which 1.0 g of graphite and 0.5 g of $NaNO_3$ were added, and the mixture was stirred at a temperature below 5 °C. Afterward, 3.0 g of $KMnO_4$ was gradually added to the mixture for 2 hours at a temperature below 10 °C for the oxidation reaction. Once the mixture turned green, 23 mL of distilled water was slowly added, and the mixture was heated to 90 °C. Afterward, 120 mL of distilled water was added before the mixture was cooled to less than 50 °C, after which 10 mL of H_2O_2 was added, and the sample was allowed to settle overnight. After the suspension had settled, the water was removed, and 400 mL of 5 wt% HCl was added while thorough stirring was maintained. The mixture subsequently settled once more. Later, the upper water layer was removed, and the suspension mixture was isolated by centrifugation until a neutral pH was reached. The mixture was finally dried at 60 °C for 12 hours to yield the GO powder.

rGO was synthesized from as-prepared GO by a reduction process with ascorbic acid as the reducing agent (Andrijanto et al., 2016). The solid GO was first dispersed in distilled water and sonicated thoroughly to obtain a suspension. The suspension was heated to 65 °C, and ascorbic acid was added in an amount ten times the mass of the GO. The reaction mixture was maintained at 65 °C for 1 hour, during which time the color changed from brown to black, indicating the reduction of GO to rGO. The resulting product was filtered and repeatedly washed with distilled water until it was neutralized. Finally, the solid was dried at 60 °C for 12 hours to obtain the rGO powder.

2.2) Synthesis of FM/rGO

FM/rGO was fabricated by a coprecipitation method, following a previous procedure (Kumar et al., 2020). First, an equimolar amount of each as-prepared $Fe(NO_3)_3$ (10 mL, 0.5 mol L^{-1}) and $Mn(NO_3)_2$ (10 mL, 0.5 mol L^{-1}) solution as the precursors was added to a 100-mL beaker containing 20 mL of 5 wt% PVA solution. The mixture was vigorously stirred at 80 °C on a magnetic stirrer. To follow, 28 mg of the rGO carrier (5 wt%) was dispersed into the mixture before the NaOH (2 mol L^{-1}) solution was added dropwise (until the pH was 12) to promote the precipitation of Fe^{3+} and Mn^{2+}. The mixture was stirred for the next hour. The solid was subsequently collected by filtration, washed several times with distilled water, and dried at 60 °C. Finally, the dried powder was exposed to microwave irradiation (800 W, 2450 MHz) for 5 min to achieve the desired composites. Fe_2O_3 and Mn_2O_3 were prepared using a similar procedure for comparison.

3) Material characterization

The thermal behavior of the FM/rGO sample was analyzed using LabsysEvo by SETARAM (France). A scanning electron microscope (SEM) (Hitachi S4800, Japan) equipped with energy-dispersive X-ray spectroscopy (EDX) was utilized to examine the morphology and conduct elemental analysis of the produced catalysts. An X-ray diffractometer (Bruker, Germany) using Cu Kα beams was used to study the crystallography of the catalysts. The light absorption of the composite was evaluated using diffuse reflectance spectroscopy (DRS) on a JASCO V500 spectrometer (Japan). The photoluminescence behaviors of the samples were elucidated using a Horiba spectrometer (iHR500 model, Japan) with an excitation wavelength of 325 nm. The surface areas (SBET) of the materials were derived from the nitrogen adsorption/desorption data at −196 °C measured at an Autosorb IQ Station on the basis of the Brunauer–Emmett–Teller (BET) equation. Electrochemical impedance spectroscopy (EIS) in a 0.1 mol L^{-1} Na_2SO_4 solution was conducted using a Biologic SP-300 potentiostat (French) with a working electrode of a glassy carbon electrode (1 cm × 1 cm) mounted with the photocatalyst, a reference electrode of platinum wire, and Ag/AgCl reference electrodes.

4) Investigation of parathion degradation

Irradiation experiments were conducted in a 500 mL Pyrex UV reactor (ACE glass, U.S.A.) with a 450-W low-pressure Hg-vapor lamp placed inside and a UV filter (for visible light simulation). A water stream covered the outside of the reactor to maintain the reactor temperature at 30–35 °C. The light intensities on the exterior arc surface of the lamp and the well are 1.04 and 0.37 W cm^{-2}, respectively. The photocatalyst (1 g L^{-1}) was then dispersed into 250 mL of the parathion solution (10 ppm) without pH adjustment and magnetically stirred in the dark for 4 hours to achieve adsorption–desorption equilibrium prior to illumination. During photocatalysis, 5 mL of each sample was withdrawn every 15 min for FM/rGO and every 30 minutes for the other samples and filtered (0.45 µm) to remove the catalyst residue. The parathion concentrations in the extract were determined using gas chromatography coupled with mass spectrometry (GC/MS) (Agilent 6890). The degradation efficiency of parathion was calculated according to Eq. 1.

$$\mathbf{H}\,(\%) = ((\mathbf{C_0} - \mathbf{C_t})/\mathbf{C_0}) \times \mathbf{100}\% = ((\mathbf{S_0} - \mathbf{S_t})/\mathbf{S_0}) \times \mathbf{100}\% \qquad \text{(Eq.1)}$$

where S_0 and S_t are the peak areas of parathion on GC/MS at 0 and t min, respectively, and C_0 and C_t are the corresponding parathion concentrations. Additionally, the total organic content of the extract aliquot was also assessed on a TOC analyzer (OI Analytical Aurora 1030).

Results and discussion

1) Materials characterization

The thermal behavior of the FM/rGO sample was elucidated via simultaneous thermogravimetric analysis (TGA) and differential scanning calorimetry (DSC) (Figure 1). The TGA curve (black line) reveals a continuous mass loss with three distinct stages. The initial decrease below 300 °C can be ascribed to the evaporation of adsorbed water and volatile components. A more pronounced mass reduction occurring between 300 and 400 °C is associated with the initial decomposition of carbonaceous species or unstable intermediates, typically graphitic residues, which is further supported by a heat change in the DSC curve. The most significant transformation is observed in the range of 500–600 °C, where a strong exothermic peak is detected in the DSC curve (red line), corresponding to major combustion of rGO, oxidation, or possible crystallization processes of oxide nanoparticles. Beyond this temperature, the sample continues to undergo gradual weight loss until it stabilizes at approximately 20% of its original mass, indicating the presence of thermally stable inorganic residues, including iron and manganese oxide. These results were also in agreement with those of previous studies (Farah et al., 2020; Walter et al., 2001).

2) Photocatalytic degradation of parathion on FM /rGO

The formation and crystallization of the material were characterized by XRD data (Figure 2). The diffraction peaks of all the components, including iron oxide, man-ganese oxide, and rGO, were observed in the curve of FM/rGO. The characteristic peaks at 24.7°, 32.3°, 36.1°, and 50.8° corresponded to the hematite

phase (α-Fe_2O_3) (JCPDS Cards No. 79-0007), which was in agreement with the results of other studies21. Additionally, the specific peaks at 28.8°, 32.3°, 37.8°, 44.5°, 50.7°, and 64.7° were attributed to the diffraction planes of Mn_2O_3 nanoparticles (JCPDS card No. 71-0636) in a tetragonal structure, as reported by previous authors (Ren et al., 2018; Thota et al., 2010). In addition, other strange peaks at 36.1°, 58.6° and 60.5° were aligned with the diffraction patterns of Mn3O4 in the FM/rGO sample (JCPDS Card No.00-001-1127) (Ullah et al., 2017). The presence of Mn_3O_4 might be due to partial reduction with carbonaceous materials, such as rGO and PVA, in the precursor mixture. Moreover, the peak at 26.0° aligned to graphitic C–C bonds and a π-conjugated structure ascribed to rGO in the FM/rGO composite (Hidayah et al., 2017). The occurrence of signal overlap between Fe_2O_3 and Mn_2O_3, as well as Mn_3O_4, was also observed. By using the Scherrer equation (Mustapha et al., 2019), the sizes of immobilized Fe_2O_3 and Mn_2O_3 can be calculated from their corresponding diffraction peaks, which have values of 10.49–13.25 nm and 13.49–15.81 nm, respectively. Compared with those of single-phase Fe_2O_3 (14.01–27.65 nm) and Mn_2O_3 (25.18–30.38 nm), a significant reduction and greater uniformity in particle size were observed, suggesting that the suppression of nanoparticle aggregation was dispersed on a high-surface-area carrier.

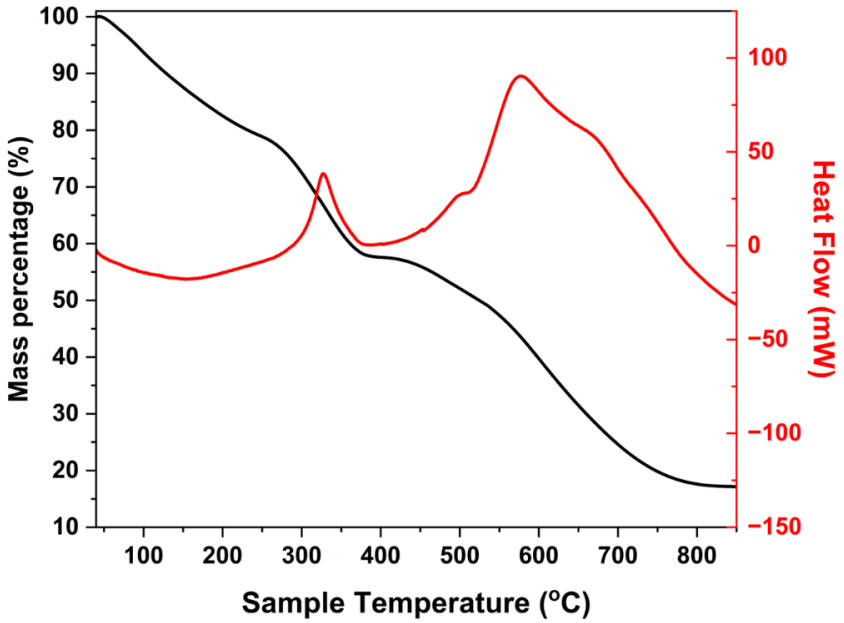

Figure 1 Thermal analysis of the FM/rGO materials.

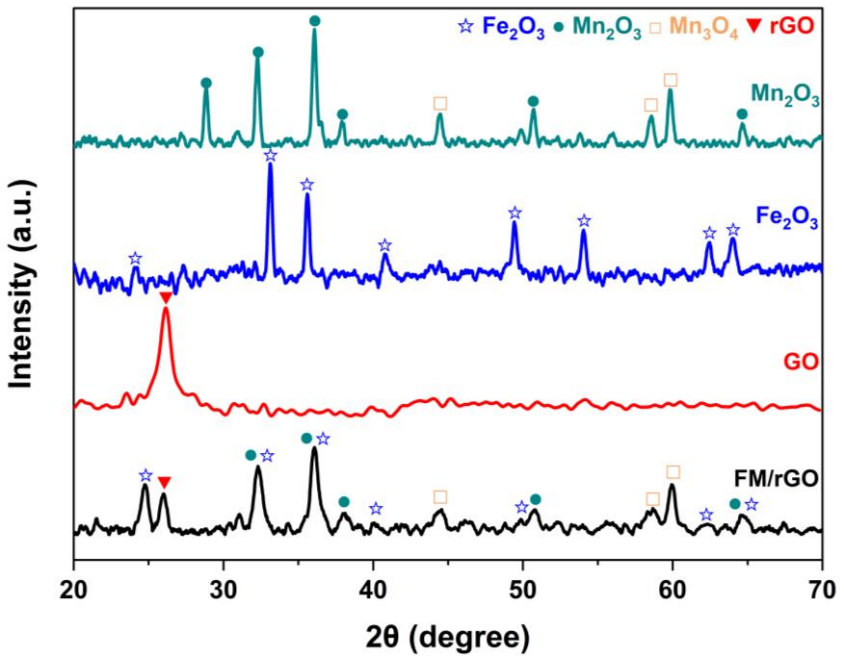

Figure 2 XRD of the FM/rGO composite.

SEM images of individual Fe_2O_3, Mn_2O_3, rGO, and FM/rGO are shown in Figure 3. The FM/rGO sample has spherical Fe_2O_3/ Mn_2O_3nanoparticles that are well distributed on the rGO surface. Mn_2O_3 is present because Fe_2O_3 has a stick-shaped structure, but in FM/rGO, it combines with Mn_2O_3 molecules to form spherical-shaped nanoparticles. During the preparation step, the various functional groups on rGO, such as >C=O and –COOH, coordinate with Fe^{3+} and Mn^{2+} precursors, thereby promoting the homogeneous growth of crystal seeds across the rGO surface (Wang et al., 2010). This uniform distribution favors crystal growth over the entire support rather than at localized sites, effectively suppressing the bulk aggregation of Fe_2O_3 and Mn_2O_3. Consequently, the resulting oxide nanoparticles exhibit a reduced particle size and more uniform morphology, which is further associated with the discussed XRD results.

In addition, the EDS method was applied to identify the included elements on the surface of the material (Figure 5(a)). The intensity of the carbon signal was considerably greater than that of the other detected elements, approximately 74.39%. Moreover, the elemental mapping images clearly demonstrated that both Fe_2O_3 and Mn_2O_3 were uniformly distributed across the surface of the rGO support with an equimolar Fe:Mn ratio, which was analogous to that in the feeding (Figure 5(b)).

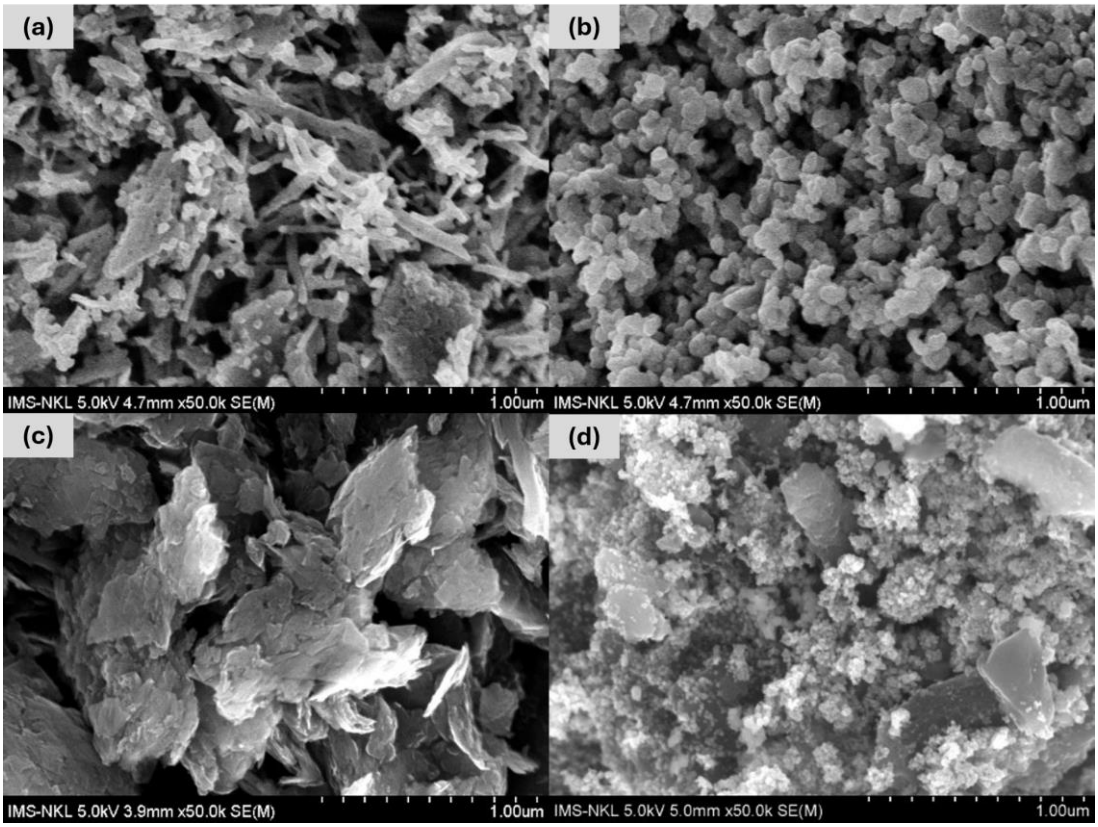

Figure 3 SEM images of (a) Fe_2O_3, (b) Mn_2O_3, (c) rGO, and (d) FM/rGO.

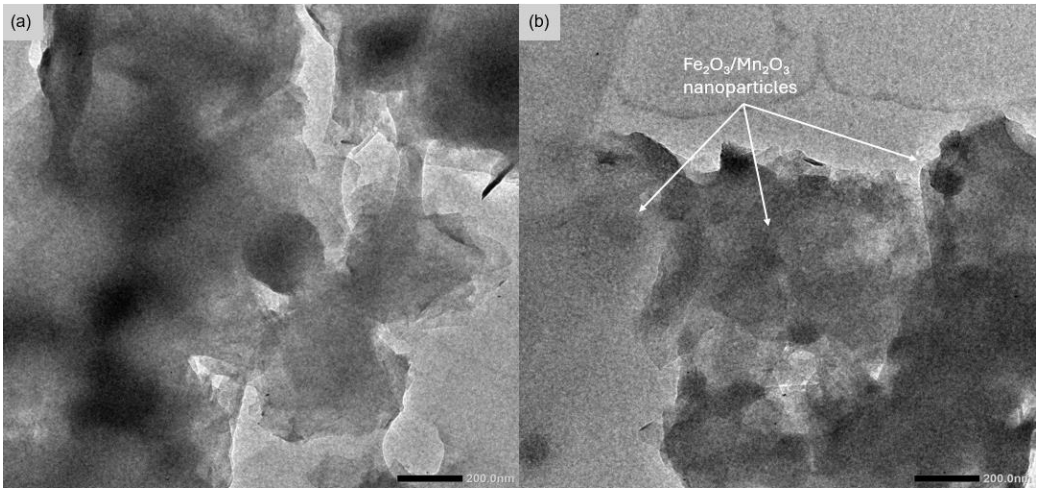

Figure 4 TEM images of (a) rGO and (b) FM/rGO.

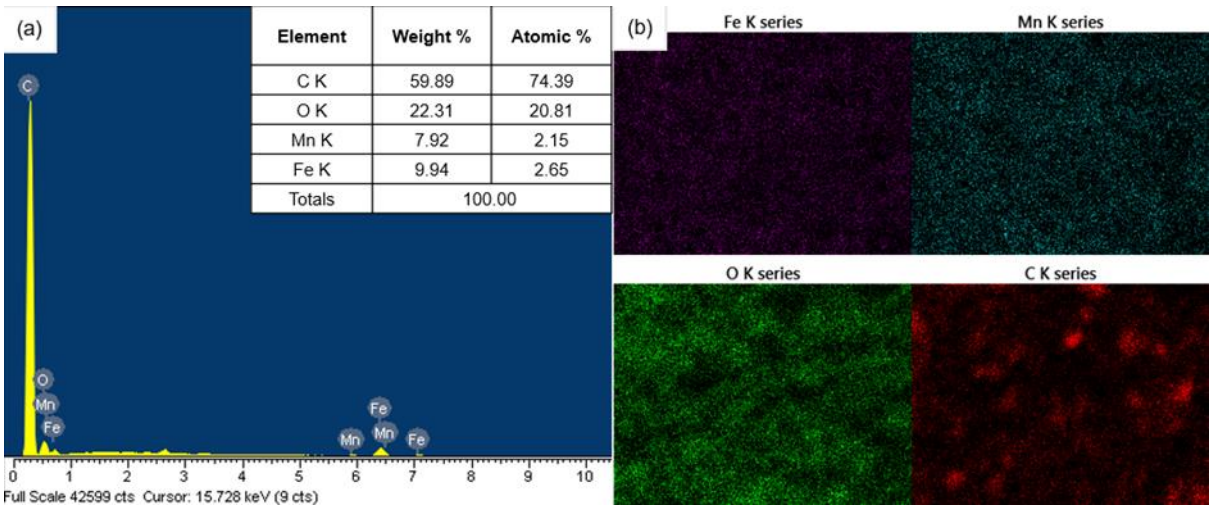

Figure 5 (a) EDS analysis and (b) elemental mapping of the FM/rGO sample.

The UV–Vis DRS method was applied to examine the optical absorption of the prepared materials (Figure 6(a)). The absorption spectrum of FM/rGO exhibits peaks at approximately 380 nm, 480 nm, and 650 nm. Notably, the first peak at 380 nm corresponds to the charac-teristic absorption of rGO. These results indicate that the FM/rGO composite is capable of absorbing both ultraviolet and visible light. Furthermore, the optical band gap of FM/rGO was derived from the Tauc equation (Eq. 2).

$$(\alpha h\nu)^{1/2} = A(h\nu - E_g) \quad \text{(Eq.2)}$$

In the Tauc plot (Figure 6a), compared with the blue curve, the observed value of 3.09 eV in the composite (red line) can be attributed to the absorption range of rGO27. Moreover, compared with those of bare Fe_2O_3 and Mn_2O_3, the band gaps at 1.82 eV and 2.25 eV correspond to nanosized Mn_2O_3 and Fe_2O_3, respectively, which positively shift (Supplementary Figure 1). The shift in the bandgap can be ascribed to surface resonance effects as Fe_2O_3 and Mn_2O_3 nanoparticles bond to oxygen-containing groups such as >C=O or –OH on the rGO surface, resulting in a higher-energy electronic transition (Solomon et al., 2020).

The optical properties of FM/rGO were also characterized using photoluminescence studies to examine the recombination of electron–hole pairs on the material surface (Figure 6(b)). PL spectra and Fe_2O_3 and Mn_2O_3 demonstrate broad and strong emission both from 400 to 700 nm and centered at approximately 520 nm, which is also near the visible light absorption described in the DRS curves, demonstrating a high recombination rate of charge carriers on the semiconductors. In contrast, the PL intensity significantly decreased by two times as the Fe_2O_3 and Mn_2O_3 nanoparticles were well decorated on the rGO support. These results indicated that the π-conjugated bonds of rGO, possibly trapping the electrons, effectively limited their recombination with the holes in the composites.

The EIS Nyquist plots of the Fe_2O_3, Mn_2O_3, and FM/rGO photocatalysts are shown in Figure 7(a). All the examined samples present a close semicircle followed by a linear tail, indicating that interfacial charge transfer and ion diffusion jointly control the electrochemical response. The EIS results reveal a progressive increase in the charge-transfer properties since the semicircle radii of Fe_2O_3 and Mn_2O_3 significantly decreased with the formation of the FM/rGO photocatalyst. This improvement can be attributed to the ability of the conductive rGO network to function with oxygen-containing groups and π-bonding as well as the formation of a heterojunction between Fe_2O_3 and Mn_2O_3, which together promote electron transport and suppress charge accumulation at the interface. Therefore, compared with that of both bare Fe_2O_3 and Mn_2O_3 photocatalysts, the photocatalytic performance of FM /rGO is expected to be significantly enhanced.

Nitrogen adsorption/desorption in combination with the BET equation was employed to determine the SBET value of the prepared composite (Figure 7(b)). The examined samples demonstrated type IV isotherms with H_3 hysteresis loops of Fe_2O_3 and Mn_2O_3 and H_4 hysteresis loops for FM/rGO, which commonly characterize the presence of carbonaceous materials (rGO) in the composite (Fan et al., 2015). The loops of Fe_2O_3 and Mn_2O_3 began to form at a p/po of 0.45, whereas that of the FM/rGO composite started early at 0.42. The behaviors of the nitrogen adsorption curves also indicated the mesoporous structures of the investigated samples. Furthermore, the derived SBET of those samples increased in the order of Fe_2O_3 (25.6 $m^2\ g^{-1}$) < Mn_2O_3 (54.2 $m^2\ g^{-1}$) < FM/rGO (394.4 $m^2\ g^{-1}$). These results indicate that the role of the rGO support is to significantly increase the capacity of contaminants to adsorb onto the composite, consequently facilitating the interaction between Fe_2O_3 and the Mn_2O_3 photocatalytic center for later parathion degradation.

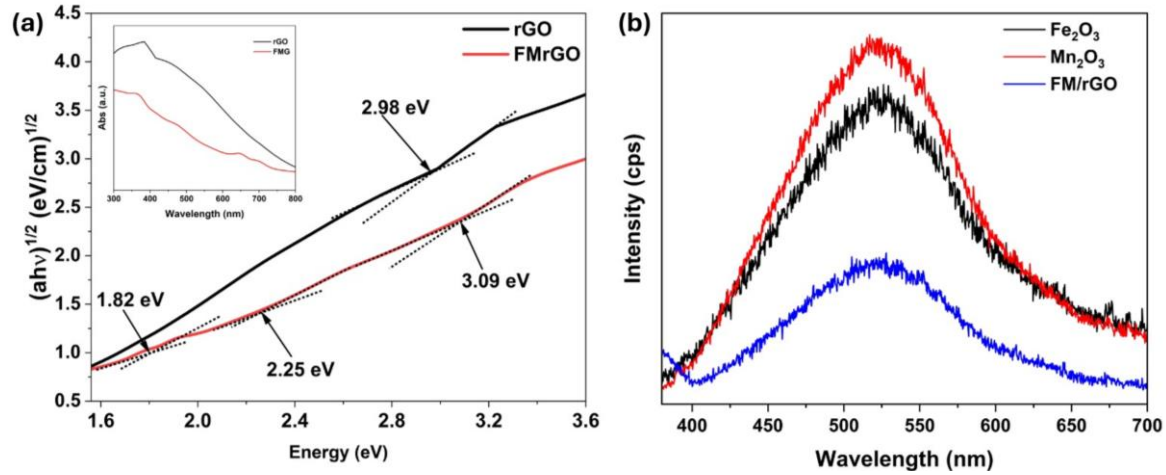

Figure 6 (a) Tauc plot (inset: the corresponding DRS curves) and (b) PL spectra of the examined samples.

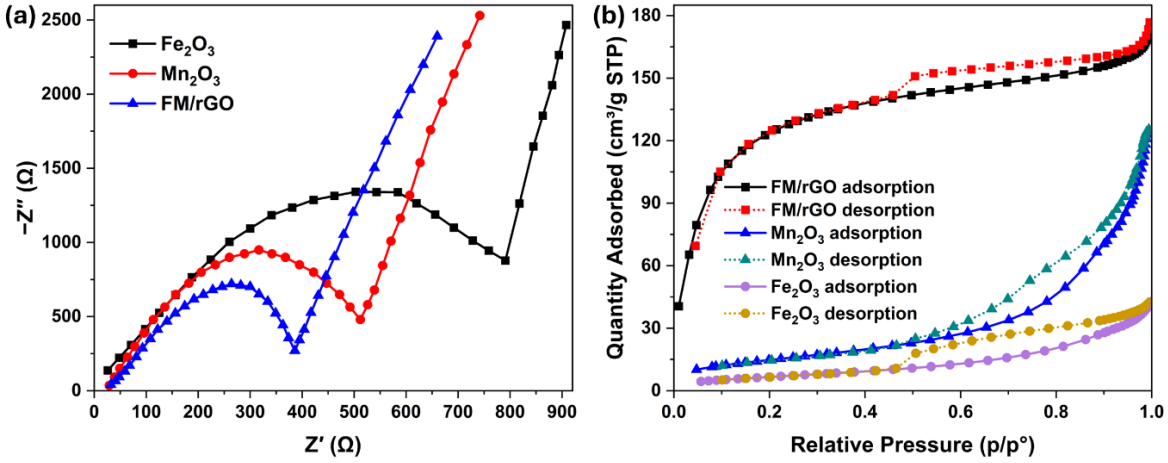

Figure 7 (a) EIS and (b) nitrogen adsorption/desorption curves of the prepared samples.

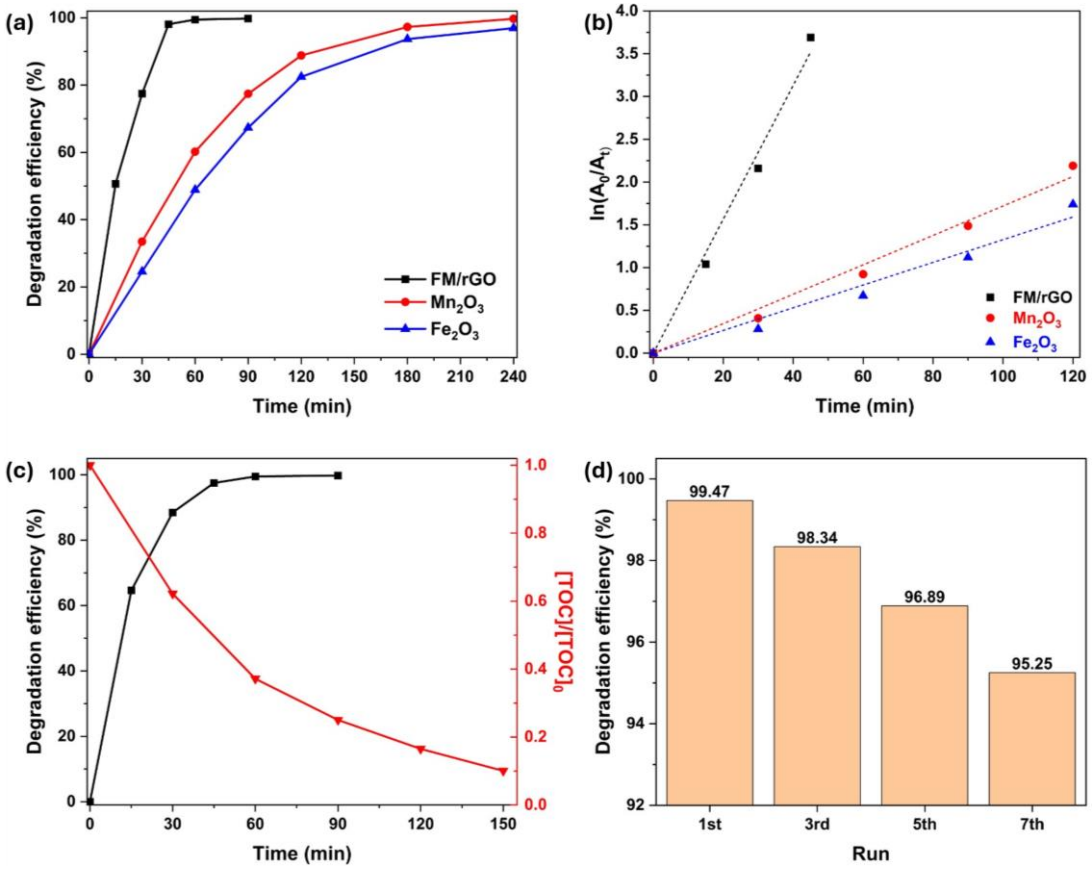

Figure 8 (a) Parathion photodegradation, (b) kinetic study, (c) TOC removal, and (d) reusability test using the FM/rGO composite.

In this section, the photocatalytic performance of FM/rGO was investigated in a parathion degradation experiment and compared to that of Fe_2O_3 and Mn_2O_3. Compared with those of Fe_2O_3 and Mn_2O_3, the parathion degradation efficiency of FM/rGO was significantly greater. After the first 45 minutes, nearly 100% of the initial parathion was completely degraded by the FM/rGO photocatalyst. In contrast, the single-component semiconductors Mn_2O_3 and Fe_2O_3 required approximately 150 minutes to reach a degradation efficiency of approximately 90% and up to 240 minutes to achieve 99.70% and 96.92%, respectively. To complement this, the kinetic plots obtained using a pseudo-first-order kinetic model, $\ln(A_0/A_t) = kt$, were used to determine the reaction rate k, as described in Figure 7(b). The parathion degradation rate k (with a linear regression $R^2 \approx 0.99$ for the fitting lines) increased in the order of Fe_2O_3 (0.0133 min^{-1}) < Mn_2O_3 (0.0172 min^{-1}) < FM/rGO (0.0782 min^{-1}). The significant increase in the degradation rate suggested the effective enhancement of the photocatalytic performance as the Fe_2O_3 and Mn_2O_3 nanoparticles were decorated on the rGO support. The promotion effect of the parathion treatment on the FM/rGO composite can be explained by (i) the increase in the surface area of the composite as well as the increase in light absorption, (ii) the uniform dispersion of Fe_2O_3 and Mn_2O_3 nanoparticles, which mitigated aggregation and released more catalytic active sites, and (iii) the suppression of charge recombination in the presence of π-conjugated bonds, which resulted in a high surface area (Li et al., 2016).

In addition, the mineralization of parathion using FM /rGO was evaluated on the basis of the change in the TOC content (Figure 7(c)). Although the degradation efficiency reached approximately 98% at 45 minutes, the TOC removal reached only approximately 75% at 90 minutes, suggesting the presence of various intermediates during photocatalysis that slowed the reaction. After 150 minutes of illumination, the TOC removal ultimately approached approximately 90%, still indicating a good degree of mineralization for parathion photodegradation using the FM/rGO composite. Moreover, the reusability of the material was evaluated by performing successive photocatalytic reactions with the same catalyst. The results, as presented in Figure 7(d), demonstrated good durability: after seven degradation cycles of parathion, the FM/rGO material retained a decomposition efficiency of up to 95.25%, with only a near 5% reduction during the first cycle.

The conduction band (CB) and valence band (VB) energy potentials can be obtained from Eqs. 3 and 4:

$$E_{VB} = x - E_f + 0.5 \times E_g \quad \text{(Eq.3)}$$

$$E_{CB} = E_{VB} - E_g \quad \text{(Eq.4)}$$

where χ represents the electronegativity of the semiconductor on the Mulliken scale [$\chi(Fe_2O_3)$ = 5.87 eV; $\chi(Mn_2O_3)$ = 5.68 eV] and E_f is the free electron energy on the hydrogen electrode scale (4.5 eV). Therefore, on the basis of the DRS data, the calculated $E_{VB}(Fe_2O_3)$, $E_{CB}(Fe_2O_3)$, $E_{VB}(Mn_2O_3)$, and $E_{CB}(Mn_2O_3)$ were 2.50 eV, 0.25 eV, 2.09 eV, and 0.27 eV, respectively. The results revealed the formation of a type-I (straddling) heterogeneous photocatalyst system on the prepared composite, which was in agreement with previous studies (Baek et al., 2022, Ghaffari et al., 2020). Under solar light irradiation, both Fe_2O_3 and Mn_2O_3 can efficiently absorb light energy to generate lectrons and holes. The formation of heterogeneous photocatalysts between Fe_2O_3 and Mn_2O_3 subsequently facilitated charge transport on the surface of the materials as electrons possibly moved from $CB(Fe_2O_3)$ to $CB(Mn_2O_3)$, where photogenerated holes were transferred from the $VB(Fe_2O_3)$ to the $VB(Mn_2O_3)$ (Li et al., 2015). Moreover, because the standard redox potential of $\bullet O_2^-/O_2$ was more negative than those of $ECB(Fe_2O_3)$ and $ECB(Mn_2O_3)$, the formation of $\bullet O_2^-$ radicals on the composite was thermodynamically unfavorable. On the other hand, because only $EVB(Fe_2O_3)$ was more positive than the standard redox potential of $H_2O/\bullet OH$, •OH was more likely to form on the $VB(Fe_2O_3)$ for the degradation of parathion than on the $VB(Mn_2O_3)$. In addition, the excited electron can reduce Fe^{3+}/Mn^{3+} to Fe^{2+}/Mn^{2+} and be captured by π-bonds on the rGO support to suppress electron/hole recombination. A plausible mechanism for parathion photodegradation is proposed in Figure 9 and described by Eqs. 5 to 10.

$$Fe_2O_3 + Mn_2O_3 + h\nu \rightarrow Fe_2O_3(e^- + h^+) + Mn_2O_3(e^- + h^+) \quad \text{(Eq. 5)}$$

$$Fe_2O_3(e^-) \rightarrow Mn_2O_3(e^-) \quad \text{(Eq. 6)}$$

$$Fe_2O_3(h^+) \rightarrow Mn_2O_3(h^+) \quad \text{(Eq. 7)}$$

$$Fe_2O_3(h^+) + H_2O \rightarrow \bullet OH + H^+ \quad \text{(Eq. 8)}$$

$$Fe^{3+}(\text{or } Mn^{3+}) + e^- \rightarrow Fe^{2+}(\text{or } Mn^{2+}) \quad \text{(Eq. 9)}$$

$$e^- + h^+ + \bullet OH + \text{parathion} \rightarrow \text{intermediates} \rightarrow \text{mineralized products} \quad \text{(Eq. 10)}$$

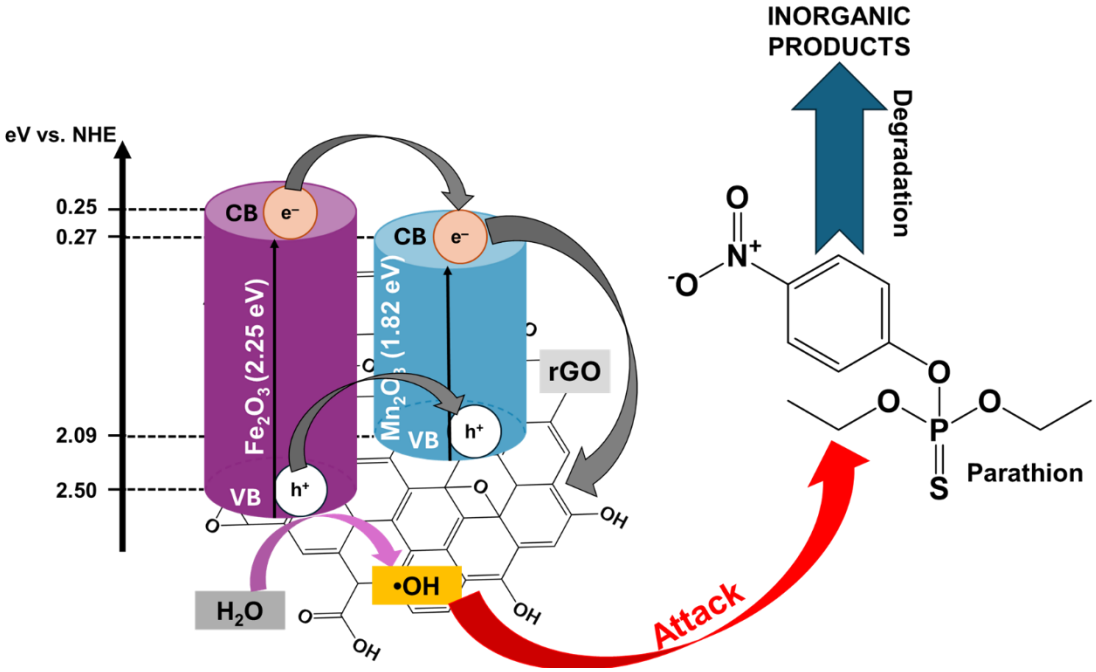

Figure 9 Proposed photodegradation of parathion on FM/rGO.

Conclusions

The low-cost, environmentally friendly, and easily synthesized photocatalyst FM/rGO was successfully prepared from $Fe(NO_3)_3$ and $Mn(NO_3)_2$ precursors using the coprecipitation method with the assistance of microwave irradiation. Material characterization of the FM/rGO sample confirmed the presence of anchored α-Fe_2O_3 and tetragonal Mn_2O_3 particles with an equi-molar ratio well dispersed on the rGO surface. The DRS results demonstrated good visible light absorption with a bandgap of 2.25 eV, whereas the PL spectra revealed a reduction in the electron–hole recombination rate as the Fe_2O_3 and Mn_2O_3 nanoparticles were immobilized on the rGO carrier. Photocatalytic experiments demonstrated that FM/rGO at a dosage of 1 g L^{-1} was able to rapidly degrade 250 mL of 10 ppm parathion in neutral media under simulated visible light, achieving a degradation efficiency of approximately 100% after 60 min and a mineralization of approximately 90% after 150 minutes. Even after seven cycles, the material maintained a high efficiency of 95.25%. These findings indicate that the degradation of the pesticide parathion was effectively facilitated on the FM/rGO material.

Acknowledgements

This study is supported by the Vietnam Academy of Science and Technology under grant number VAST 03.05/25-26.

Data availability statement

Information and data used in the study will be disclosed upon request.

Author ORCID

Nguyen Q. Bac: 0000-0003-2663-9710
Dao N. Nhiem: 0000-0002-7769-3701
Nguyen T. Kien: 0000-0001-5213-3882

Author contributions

Nguyen V. N. Mai: Formal analysis, Investigation, Data curation,
Pham N. Chuc: Validation, Project administration, Funding acquisition
Nguyen H. Chi: Formal analysis, Investigation, Writing – Original draft
Nguyen M. Phuong: Conceptualization, Methodology, Supervision
Nguyen Q. Bac: Software, Investigation, Visualization
Nguyen T. H. Chi: Formal analysis, Investigation, Data curation
Dao N. Nhiem: Investigation, Resources, Data curation
Nguyen T. Kien: Software, Formal analysis, Writing – Review & editing

Conflicts of interest

The authors declare that there are no conflicts of interest in competing financial or personal relationships that could have appeared to influence the work reported in this work.

References

Ahmad, F., & Mehmood, M. (2022). A critical review of photocatalytic degradation of organophosphorus pesticide “Parathion” by different mixed metal oxides.

Advanced Journal of Chemistry, Section A, *5(*4), 287–310.

Andrijanto, E., Shoelarta, S., Subiy anto, G., & Rifki, S. (2016). Facile synthesis of graphene from graphite using ascorbic acid as reducing agent. *AIP Conference Proceedings*, *1725*, 020003.

Baek, S., Ghaffari, Y., & Bae, J. (2022). Synthesis of Fe_2O_3/Mn_2O_3 nanocomposites and impregnated porous dilicates for dye removal: Insights into treatment mechanisms *Catalysts*, *12*(9), 1045.

Choudhary, S., Bisht, A., & Mohapatra, S. (2021). Microwave-assisted synthesis of α-Fe_2O_3/$ZnFe_2O_4$/ZnO ternary hybrid nanostructures for photocatalytic applications. *Ceramics International*, *47*(3), 3833–3841.

Fan, C., Nguyen, V., Zeng, Y., Phadungbut, P., Horikawa, T., Do, D. D.,Nicholson, D. (2015). Novel approach to the characterization of the pore structure and surface chemistry of porous carbon with Ar, N_2, H_2O and CH_3OH adsorption. *Microporous and Mesoporous Materials*, *209*, 79–89.

Farah, S., Farkas, A., Madarasz, J., & Laszlo, K. (2020). Comparison of thermally and chemically reduced graphene oxides by thermal analysis and Raman spectroscopy. *Journal of Thermal Analysis and Calorimetry*, *142*, 331–337.

Ghaffari, Y., Gupta, N. K., Bae, J., & Kim, K. S. (2020). One-step fabrication of Fe_2O_3/Mn_2O_3 nanocomposite for rapid photodegradation of organic dyes at neutral pH. *Journal of Molecular Liquids*, *315*, 113691.

Herrmann, J. M., & Guillard, C. (2000). Photocatalytic degradation of pesticides in agricultural used waters. *Comptes Rendus l'Académie des Sciences – Series IIC - Chemistry*, *3*, 417–422.

Hidayah, N. M. S., Liu, W. W., Lai, C. W., Noriman, N. Z., Khe, C. S., Hashim, U., & Lee, H. C. (2017). Comparison on graphite, graphene oxide and reduced graphene oxide: Synthesis and characterization. *AIP Conference Proceedings*, *1892*, 150002.

Li, H., Zhou, Y., Tu, W., Ye, J., & Zou, Z. (2015). State-of-the-art progress in diverse heterostructured photocatalysts toward promoting photocatalytic performance. *Advances Functional Materials*, *25*(7), 998–1013.

Jha, B. K., Chaule, S., & Jang, J. H. (2024). Enhancing photocatalytic efficiency with hematite photoanodes: Principles, properties, and strategies for surface, bulk, and interface charge transfer improvement. *Materials Chemistry Frontiers*, *8*, 2197–2226.

Jha, B. K., & Jang, J. H. (2025). Beyond single dopants: The chemistry of multi-atom doping in hematite photoanodes for water splitting. *ACS Applied Materials & Interfaces*, *17*(35), 49079–49091.

Kim, T. S., Kim, J. K., Choi, K., Stenstrom, M. K., & Zoh, K. D. (2006). Degradation mechanism and the toxicity assessment in TiO_2 photocatalysis and photolysis of parathion. *Chemosphere*, *62*(6), 926–933.

Kumar, R., Yourssry, S. M., Ya, K. Z., Tan, W. K., Kawamura, G., & Matsuda, A. (2020). Microwave-assisted synthesis of Mn_3O_4-Fe_2O_3/Fe_3O_4@rGO ternary hybrids and electrochemical performance for supercapacitor electrode. *Diamond and Related Materials*, *101*, 107622.

Le, H. B., Nguyen, K. T., Nghiem, T. X., Nguyen, B. Q., Nguyen, C. T. H., Pham, C. N., Nguyen, T. K., & Dao, N. N. (2024). Efficient photocatalytic remediation of persistent organic pollutants using magnetically recoverable spinel manganese ferrite nanoparticles supported on activated carbon. *Materials Research Bulletin*, *178*, 112913.

Li, Z., Yu, J., Wageh, S., Al-Ghamdi, A. A., & Xie, J. (2016). Graphene in photocatalysis: A review. *Nano· Micro Small*, *12*(48), 6640–6696.

Liao, X., Zhou, C., Zheng, F., & Peng, M. (2025). Methyl parathion degradation from the sulfide oxidation catalyzed by crystallographic manganese oxides: Formation and role of singlet oxygen. *Separation and Purification Technology*, *361*(1), 131325.

Loučka, T., Došek, M., & Kříženecká, S., & Janoš, P. (2018) Electrochemical behaviour and degradation of methyl parathion on platinum electrode. *Journal of Electroanalytical Chemistry*, *823*, 580–587.

Mishra, M., & Chun, D. M. (2015). α-Fe_2O_3 as a photocatalytic material: A review. *Applied Catalysis A: General*, *498*, 126–141.

Mohamed, M. A., Rahman, N. A., Zain, M. F. M., Minggu, L. J., Kassim, M. B., Jaafar, J., Samad, S., Mastuli, M. S., & Wong, R. J. (2020). Hematite microcube decorated TiO_2 nanorods as heterojunction photocatalyst with in-situ carbon doping derived from polysaccharides bio-templates hydrothermal carbonization. *Journal of Alloys and Compounds*, *820*, 153143.

Mondal, A., Prabhakaran, A., Gupta, S., Subramanian, V. R. (2021). Boosting photocatalytic activity using reduced graphene oxide (RGO)/semiconductor nanocomposites: Issues and future scope. *ACS Omega*, *6*(13), 8734–8743.

Mustapha, S., Ndamitso, M. M., Abdulkareem, A. S., Tijani, J. O., Shuaib, D. T., Mohammed, A. K., & Sumaila, A. (2019). Comparative study of crystallite size using Williamson-Hall and Debye-Scherrer plots for ZnO nanoparticles. *Advances in Natural Sciences: Nanoscience and Nanotechnology*, *10*(4), 045013.

Ren, W., Liu, D., Sun, C., Yao, X., Tan, J., Wang, C., Zhao, K., Wang, X., Li, Q., & Mai, L. (2018). Nonhierarchical heterostructured Fe_2O_3/Mn_2O_3 porous hollow spheres for enhanced lithium storage. *Nano·Micro Small*, *14*(26), 1800659.

Samal, A., Das, D. P., Madras, G. (2018). Repercussion of solid state vs. Liquid state synthesized p-n

heterojunction RGO-copper phosphate on proton reduction potential in water. *Scientific Reports*, *8*, 2881.

Singh, J., Sharma, S., Aanchal, Basu, S. (2019). Synthesis of Fe_2O_3/TiO_2 monoliths for the enhanced degradation of industrial dye and pesticide via photo-Fenton catalysis. *Journal of Photochemistry and Photobiology A: Chemistry*, 376, 32–42.

Sohail, M., Saleem, M., Ullah, S. Saeed, N., Afridi, A., Khan, M., & Arif, M. (2017). Modified and improved Hummer's synthesis of graphene oxide for capacitors applications. *Modern Electronic Materials*, *3*(3), 110–116.

Solomon, G., Kohan, M. G., Landstorm, A., Vomiero, A., Concina, I. (2020). Semiconducting metal oxides empowered by graphene and its derivatives: Progresses and critical perspective on selected functional applications. *Journal of Applied Physics*, *128*, 180905.

Thota, S., Prasad, B., & Kumar, J. (2010). Formation and magnetic behaviour of manganese oxide nanoparticles. *Materials Science and Engineering: B*, *167*(3), 153–160.

Ullah, A. K. M. A., Kibria, A. K. M. F., Akter, M., Khan, M. N. I., Tareg, A. R. M., & Firoz, S. H. (2017). Oxidative degradation of methylene blue using Mn_3O_4 nanoparticles. *Water Conservation Science and Engineering*, *1*, 249–256.

Usgodaarachchi, L., Jayanetti, M., Thambiliyagodage, C., Liyanaarachchi, H., & Vigneswaran, S. (2023). Fabrication of r-GO/GO/α-Fe_2O_3/Fe_2TiO_5 nanocomposite using natural ilmenite and graphite for efficient photocatalysis in visible light. *Materials (Basel)*, *16*(1), 139.

Walter, D., Buxbaum, G., & Laqua, W. (2001). The mechanism of the thermal transformation from goethite to hematite. *Journal of Thermal Analysis and Calorimetry*, 63, 733–748.

Wang, H., Robinson, J. T., Diankov, G., Dai, H. (2010). Nanocrystal growth on graphene with various degrees of oxidation. *Journal of the American Chemical Society*, *132*(10), 3270–3271.